

Kalman Filter-based Sensing in Communication Systems with Clock Asynchronism

Xu Chen, *Member, IEEE*, Zhiyong Feng, *Senior Member, IEEE*, J. Andrew Zhang, *Senior Member, IEEE*, Xin Yuan, *Member, IEEE*, and Ping Zhang, *Fellow, IEEE*

Abstract—In this paper, we propose a novel Kalman Filter (KF)-based uplink (UL) joint communication and sensing (JCAS) scheme, which can significantly reduce the range and location estimation errors due to the clock asynchronism between the base station (BS) and user equipment (UE). Clock asynchronism causes time-varying time offset (TO) and carrier frequency offset (CFO), leading to major challenges in uplink sensing. Unlike existing technologies, our scheme does not require knowing the location of the UE in advance, and retains the linearity of the sensing parameter estimation problem. We first estimate the angle-of-arrivals (AoAs) of multipaths and use them to spatially filter the CSI. Then, we propose a KF-based CSI enhancer that exploits the estimation of Doppler with CFO as the prior information to significantly suppress the time-varying noise-like TO terms in spatially filtered CSIs. Subsequently, we can estimate the accurate ranges of UE and the scatterers based on the KF-enhanced CSI. Finally, we identify the UE's AoA and range estimation and locate UE, then locate the dumb scatterers using the bi-static system. Simulation results validate the proposed scheme. The localization root mean square error of the proposed method is about 20 dB lower than the benchmarking scheme. a

Index Terms—Joint communications and sensing (JCAS), integrated sensing and communications (ISAC), uplink localization, 6G, Kalman filter.

I. INTRODUCTION

A. Backgrounds and Motivations

In the future 6G networks, communication and sensing are indispensable functions for facilitating autonomous machines, such as in intelligent vehicular networks, smart factories, and smart cities [1]–[3]. Nevertheless, the rapid proliferation of wireless devices will result in severe spectrum congestion problem [4], [5]. Joint communications and sensing (JCAS),

also known as integrated sensing and communications (ISAC), is a promising technology to solve the above problem. JCAS can achieve both sensing and communications by sharing the same transceivers and spectrum, and the same transmitted signals [6]–[9].

Referring to the perceptive mobile networks [8], sensing can be realized using both uplink (UL) and downlink (DL) signals. JCAS can achieve UL communication and bi-static sensing simultaneously, without requiring full-duplex operations as in the downlink JCAS [10]. Therefore, UL JCAS can be realized, requiring almost no changes to network infrastructure. However, the clock asynchronism between the base station (BS) and the user equipment (UE) significantly restrains the location and Doppler frequency estimation accuracy in UL JCAS. This is because the clock asynchronism leads to time-varying timing offset (TO) and carrier frequency offset (CFO), which cause sensing ambiguity and prevent the coherent processing of sensing signals. Resolving the clock asynchronism is one of the most challenging problems in UL JCAS.

B. Related Works

The CFO in the UL communication and localization can be estimated using conventional methods, and the residual CFO after the estimation and compensation is generally small. However, it is challenging to estimate and suppress the TO, as it is absorbed as part of the channel response and cannot be directly extracted from the received signals [11], [12].

For a long time, cooperation among multiple BSs and iterative localization using multiple transmissions is a common approach to dealing with the range and location offset due to TO. In [13], the authors proposed an expectation-maximization (EM)-based cooperative localization method. This method requires not only multiple receivers but also 20 EM iterations, which results in a high implementation complexity.

Recently, some new techniques have been developed to address the clock asynchronism problem. In [14], the authors proposed to use the cross-antenna cross-correlation (CACC) method to achieve passive human tracking with a single WiFi link by exploiting the cross-correlation between each pair of antennas. In [15], the authors proposed a UL JCAS method for perceptive mobile networks, allowing a static UE and BS to form a bi-static system to sense the environment by utilizing the CACC method. However, the CACC method only works under the assumption that the transmitter and receiver are static, and the accurate location of UE is known in advance. Moreover, the CACC method has to solve the

This work has been submitted to IEEE JSAC Special issue: 5G/6G Precise Positioning on Cooperative Intelligent Transportation Systems (C-ITS) and Connected Automated Vehicles (CAV)

This work is supported by the National Key Research and Development Program of China under Grants {2020YFA0711300, 2020YFA0711302, and 2020YFA0711303}, and the National Natural Science Foundation of China under Grants {61941102, 61790553}, and BUPT Excellent Ph.D. Students Foundation under grant CX2021110.

Xu Chen, Z. Feng, and Z. Wei are with Beijing University of Posts and Telecommunications, Key Laboratory of Universal Wireless Communications, Ministry of Education, Beijing 100876, P. R. China (Email: {chenxu96330, fengzy, weizhiqing}@bupt.edu.cn).

J. A. Zhang is with the Global Big Data Technologies Centre, University of Technology Sydney, Sydney, NSW, Australia (Email: Andrew.Zhang@uts.edu.au).

Ping Zhang is with Beijing University of Posts and Telecommunications, State Key Laboratory of Networking and Switching Technology, Beijing 100876, P. R. China (Email: pzhang@bupt.edu.cn).

X. Yuan is with Commonwealth Scientific and Industrial Research Organization (CSIRO), Australia (email: Xin.Yuan@data61.csiro.au).

Corresponding author: Zhiyong Feng

challenging image targets problem. In [16]–[18], the authors proposed to use the Cross-Antenna Signal Ratio (CASR) method to estimate the Doppler frequency, using the channel state information (CSI) ratio between two antennas. However, this method works only when the scatterers are static except for the target of interest in order to maintain the linearity of the sensing parameter estimation problem based on the CSI ratio.

C. Contributions

In this paper, referring to the perceptive mobile networks, we propose a novel Kalman Filter (KF)-based UL JCAS sensing scheme to accurately estimate the ranges and locations of the UE and dumb scatterers in the presence of clock asynchronism between bi-static UE and BS. Unlike existing techniques, our method does not require to know the location of the UE, and maintains the linearity of the sensing parameter estimation problem so that the conventional sensing algorithms, such as spectrum analysis techniques, can be applied.

We first use a two-dimensional (2D) multiple signal classification (MUSIC)-based angle-of-arrival (AoA) estimation method to estimate the AoAs of multipaths and form a spatial filter to separate the incident signals with different AoAs. Then, we propose a MUSIC-based decoupled range and Doppler estimation (DRDE) method to estimate DPOs and ranges. A KF-based CSI enhancer is introduced during the DRDE processing to suppress the noise-like time-varying TO terms. Finally, we propose a UL bi-static localization method to first locate UE, and subsequently locate the dumb scatterers accurately using the bi-static system.

The main contributions of this paper are summarized as follows.

1. We propose an expanded 2D MUSIC-based AoA estimation method that exploits the CSIs over all packets to estimate the accurate AoAs. Then, we use the estimated AoAs to construct a spatial filter to separate the UL communication CSIs with different AoAs. This enables to identify the UE and scatterers in different angles.
2. We propose a MUSIC-based DRDE method to decouple the estimation of Doppler frequency and range, generate the Doppler frequency plus CFO (DPO) estimates as inputs to a KF-based CSI enhancer, and obtain accurate range estimation from the output of the enhancer. Moreover, the Cramer-Rao bound (CRB) for the range estimation is derived. Note that the MUSIC-based DRDE method can share the same sensing processing module with the aforementioned MUSIC-based AoA estimation method.
3. We propose a KF-based CSI enhancer that can use the estimated DPO as the prior information for a KF to filter the CSI and suppress the time-varying noise-like phase shift due to TO. The enhancer provides refined CSI for accurate range estimation of the UE and dumb scatterers.
4. We propose a bi-static UL JCAS localization method for locating the UE and dumb scatterers. Exploiting the fact that the line-of-sight path from UE to BS is the shortest, the BS first estimates the location of UE to form a bi-static system, and then uses the bi-static system to locate

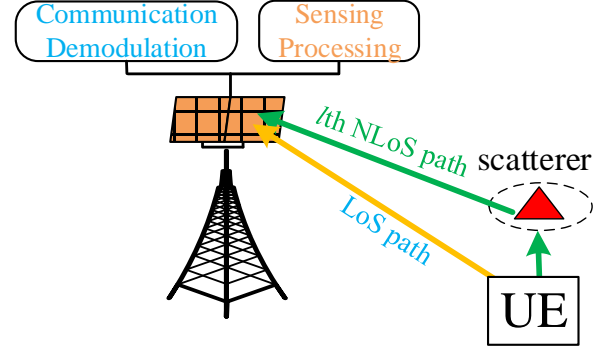


Fig. 1: The UL JCAS scenario.

the dumb scatterers based on the estimated AoAs and ranges of the scatterers.

We provide extensive simulation results, validating the proposed KF-based UL JCAS sensing scheme. The localization root mean square error (RMSE) of the proposed KF-based UL JCAS scheme is shown to be about 20 dB lower than the benchmarking scheme.

The remaining parts of this paper are organized as follows. In section II, we describe the system model of the UL JCAS scheme. Section III proposes the KF-based UL JCAS sensing scheme. Section IV analyzes the CRB and complexity of the proposed KF-based UL JCAS scheme. In section V, the simulation results are presented. Section VI concludes this paper.

Notations: Bold uppercase letters denote matrices (e.g., \mathbf{M}); bold lowercase letters denote column vectors (e.g., \mathbf{v}); scalars are denoted by normal font (e.g., γ); the entries of vectors or matrices are referred to with square brackets, for instance, the q th entry of vector \mathbf{v} is $[\mathbf{v}]_q$, and the entry of the matrix \mathbf{M} at the m th row and q th column is $[\mathbf{M}]_{m,q}$; $\mathbf{U}_s = [\mathbf{U}]_{:,N_1:N_2}$ means the matrices sliced from the N_1 th to the N_2 th columns of \mathbf{U} ; $(\cdot)^H$, $(\cdot)^*$ and $(\cdot)^T$ denote Hermitian transpose, complex conjugate and transpose, respectively; $\mathbf{M}_1 \in \mathbb{C}^{M \times N}$ and $\mathbf{M}_2 \in \mathbb{R}^{M \times N}$ are $M \times N$ complex-value and real-value matrices, respectively; $\|\mathbf{v}\|_\ell$ represents the ℓ -norm of \mathbf{v} , and ℓ_2 -norm is considered in this paper; and $v \sim \mathcal{CN}(m, \sigma^2)$ means v follows a complex Gaussian distribution with mean m and variance σ^2 .

II. SYSTEM MODEL

This section presents the UL JCAS system setup, channel model, and transmit and received signal models to provide fundamentals for UL JCAS signal processing.

A. UL JCAS System Setup

We consider a UL JCAS system where the BS and UE use uniform plane arrays (UPAs), as shown in Fig. 1. In the UL period, UE transmits the UL preamble and data signals, and BS uses the received training sequences in the preamble for CSI estimation and then conducts UL bi-static sensing. Using the estimated CSI, the BS also demodulates the UL data signals of UE. The data payload signals are not used for sensing in this paper.

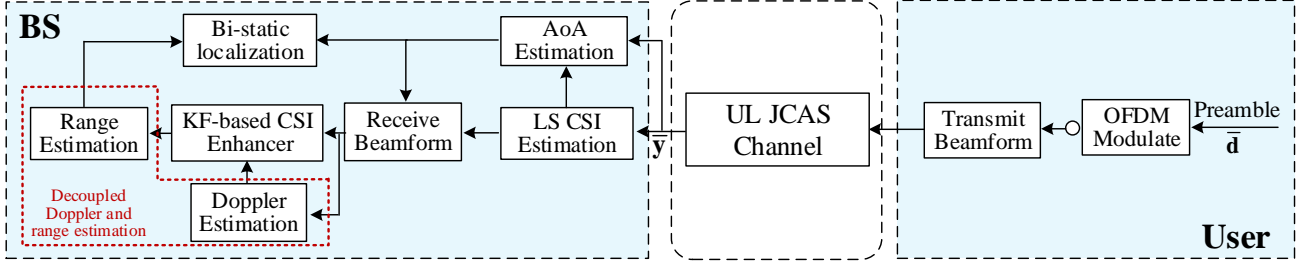


Fig. 2: The UL JCAS scheme including the KF-based JCAS CSI estimation.

For simplicity of presentation, we assume that training sequences for channel estimation are transmitted at an equal interval. Each training sequence can be part of a typical packet in, e.g., WiFi systems, or transmitted in timeslot regularly, in, e.g., 5G mobile networks. For the simplicity of notation, we refer to the packet structure in this paper, and there is one channel estimate from each packet. We also assume that within a coherent processing interval (CPI), M_s CSI estimates are obtained and used for sensing, at an interval of T_s^p . The key idea in this paper can be extended to more general cases of non-uniform intervals.

Orthogonal frequency division multiplexing (OFDM) signal is used. The key parameters for the OFDM signal are denoted as follows. P_t^U is the transmit power, N_c is the number of subcarriers occupied by UE in each OFDM symbol; f_c is the carrier frequency, and Δf is the subcarrier interval.

B. UPA Model

The uniform interval between neighboring antenna elements is denoted by d_a . The size of UPA is $P \times Q$. The AoA for receiving or the angle-of-departure (AoD) for transmitting the k th far-field signal is $\mathbf{p}_k = (\varphi_k, \theta_k)^T$, where φ_k and θ_k are the azimuth angle and elevation angle, respectively. The phase difference between the (p,q) th antenna element and the reference antenna element is [19]

$$a_{p,q}(\mathbf{p}_k) = \exp[-j \frac{2\pi}{\lambda} d_a (p \cos \varphi_k \sin \theta_k + q \sin \varphi_k \sin \theta_k)], \quad (1)$$

where $\lambda = c/f_c$ is the wavelength of the carrier, f_c is the carrier frequency, and c is the speed of light. The steering vector for the array is given by

$$\mathbf{a}(\mathbf{p}_k) = [a_{p,q}(\mathbf{p}_k)]_{p=0,1,\dots,P-1;q=0,1,\dots,Q-1}, \quad (2)$$

where $\mathbf{a}(\mathbf{p}_k) \in \mathbb{C}^{PQ \times 1}$, and $[v_{p,q}]_{(p,q) \in \mathbf{S}_1 \times \mathbf{S}_2}$ denotes the vector stacked by values $v_{p,q}$ satisfying $p \in \mathbf{S}_1$ and $q \in \mathbf{S}_2$. The sizes of the antenna arrays of the BS and user are $P_t \times Q_t$ and $P_r \times Q_r$, respectively.

C. UL JCAS Channel Model

In this paper, we only consider propagation paths with no more than one hop, for the sake of localization. Paths with two or more hops have significantly lower power and are ignored. We assume there exists an LoS path between UE and BS. To separate different segments of a non-LoS (NLoS) path, we use subscript 1 for variables to denote the segment between

UE and a scatterer and subscript 2 for the one between the scatterer and BS. For the LoS path, we use subscript 1 only.

The UL JCAS channel response at the n th subcarrier of the m th packet is given by [11]

$$\mathbf{H}_{C,n,m} = \sum_{k=0}^{K-1} \left[b_{C,k} e^{j2\pi f_{c,d,k} m T_s} e^{-j2\pi n \Delta f \tau_{c,k}} \right] \times \mathbf{a}(\mathbf{p}_{R,k}^U) \mathbf{a}^T(\mathbf{p}_{T,k}^U), \quad (3)$$

where $\mathbf{H}_{C,n,m} \in \mathbb{C}^{P_t Q_t \times P_r Q_r}$, $k=0$ is for the channel response of the LoS path, and $k \in \{1, \dots, K-1\}$ is for the k th non-LoS (NLoS) path; $\mathbf{a}(\mathbf{p}_{R,k}^U) \in \mathbb{C}^{P_t Q_t \times 1}$ and $\mathbf{a}(\mathbf{p}_{T,k}^U) \in \mathbb{C}^{P_r Q_r \times 1}$ are the steering vectors for UL receiving and transmission, respectively; $\mathbf{p}_{R,k}^U$ and $\mathbf{p}_{T,k}^U$ are the corresponding AoA and AoD, respectively; $f_{c,d,0} = \frac{v_{0,1}}{\lambda}$ and $\tau_{c,0} = \frac{r_{0,1}}{c}$ are the Doppler shift and time delay between UE and BS of the LoS path, respectively, with $v_{0,1}$ and $r_{0,1}$ being the corresponding radial relative velocity and the distance, respectively; $f_{c,d,k} = f_{d,k,1} + f_{d,k,2}$ and $\tau_{c,k} = \tau_{c,k,1} + \tau_{c,k,2}$ are the aggregate Doppler shift and time delay of the k th NLoS path, respectively; $f_{d,k,1} = \frac{v_{k,1}}{\lambda}$ and $f_{d,k,2} = \frac{v_{k,2}}{\lambda}$ are the Doppler frequencies between UE and the k th scatterer, and between the k th scatterer and the BS, respectively, with $v_{k,1}$ and $v_{k,2}$ being the corresponding radial velocities; $\tau_{c,k,1} = \frac{r_{k,1}}{c}$ and $\tau_{c,k,2} = \frac{r_{k,2}}{c}$ are the time delays between UE and the k th scatterer, and between BS and the k th scatterer, respectively, with $r_{k,1}$ and $r_{k,2}$ being the corresponding distances. Moreover, $b_{C,0} = \sqrt{\frac{\lambda^2}{(4\pi r_{0,1})^2}}$ and $b_{C,k} = \sqrt{\frac{\lambda^2}{(4\pi)^3 r_{k,1}^2 r_{k,2}^2}} \beta_{C,k}$ are the attenuations of the LoS and NLoS paths, respectively, where $\beta_{C,k}$ is the reflecting factor of the k th scatterer, following $\mathcal{CN}(0, \sigma_{C\beta,k}^2)$ [20].

III. UL JCAS SENSING

In this section, We present the UL JCAS signal sensing scheme in the presence of both TO and CFO, for which a block diagram is shown in Fig. 2. We first present the estimated CSI expression using, e.g., the least-square (LS) channel estimation method. Constructing a signal correlation matrix, we show that AoA can be estimated without being impacted by TO and CFO, and then propose an expanded 2D MUSIC-based AoA estimation method. Using the estimated AoAs, we then construct a spatial filter to separate CSIs with different AoAs. We then introduce the first two steps of the DRDE method, including decoupling the estimation of Doppler frequency and range, and estimating the DPO. We further present the KF-based CSI enhancer that uses the estimated DPOs as the prior

information to suppress the time-varying noise-like TO terms in CSIs. The output from the KF-based CSI enhancer is then used to estimate the accurate ranges in the last step of DRDE. The range of the UE is identified as the smallest one among all the range estimates. Finally, BS can estimate the accurate location of the UE to form a bi-static system, based on which we propose the UL bi-static localization method to locate the scatterers.

A. CSI Estimation

The CSI may be estimated based on, e.g., the LS method using the training sequences in the preamble [21]. We assume that a transmit beamforming (BF) with the BF vector \mathbf{w}_T is used. Ignoring the details of training sequences and estimation method, we present the UL CSI estimation at the n th subcarrier of the m th packet as

$$\begin{aligned}\hat{\mathbf{h}}_{C,n,m} &= \mathbf{h}_{C,n,m} + \bar{\mathbf{n}}_{t,n,m} \in P_t Q_t \times 1 \\ &= \sqrt{P_t} \mathbf{H}_{C,n,m} \mathbf{w}_T \zeta_f \zeta_\tau + \bar{\mathbf{n}}_{t,n,m} \\ &= \sqrt{P_t} \sum_{k=0}^{K-1} \begin{bmatrix} b_{C,k} e^{j2\pi m T_s^p [f_{c,d,k} + \delta_f(m)]} \\ \times e^{-j2\pi n \Delta f [\tau_{c,k} + \delta_\tau(m)]} \\ \times \chi_{T,k} \mathbf{a}(\mathbf{p}_{R,k}^U) \end{bmatrix} + \bar{\mathbf{n}}_{t,n,m},\end{aligned}\quad (4)$$

where $\mathbf{h}_{C,n,m} = \sqrt{P_t} \mathbf{H}_{C,n,m} \mathbf{w}_T \zeta_f \zeta_\tau$ is the equivalent channel response, $\zeta_f = e^{j2\pi m T_s^p \delta_f(m)}$ and $\zeta_\tau = e^{-j2\pi n \Delta f \delta_\tau(m)}$ are the phase shifts due to CFO and TO, denoted by $\delta_f(m)$ and $\delta_\tau(m)$, respectively; $\delta_f(m)$ and $\delta_\tau(m)$ are random time-varying parameters, and are assumed to follow $\mathcal{CN}(0, \sigma_f^2)$ and $\mathcal{CN}(0, \sigma_\tau^2)$, respectively; $T_s^p = P_s T_s$ is the time duration between two CSI estimates; $\bar{\mathbf{n}}_{t,n,m} \in \mathbb{C}^{P_t Q_t \times 1}$ is the combined noise that contains Gaussian noise, and each element of $\bar{\mathbf{n}}_{t,n,m}$ follows $\mathcal{CN}(0, \sigma_n^2)$; \mathbf{w}_T is the transmit BF vector with $\|\mathbf{w}_T\|_2 = 1$, and $\chi_{T,k} = \mathbf{a}^T(\mathbf{p}_{T,k}^U) \mathbf{w}_T$ is the transmit BF gain.

According to (4), there are three sensing parameters, i.e., AoA, range, and Doppler frequency, that need to be estimated. AoA is the slowest time-varying one among the above three parameters. Moreover, we can see that $\hat{\mathbf{h}}_{C,n,m}(\hat{\mathbf{h}}_{C,n,m})^H$ does not contain $e^{j2\pi m T_s^p [f_{c,d,k} + \delta_f(m)]} e^{-j2\pi n \Delta f [\tau_{c,k} + \delta_\tau(m)]}$. Therefore, the AoA estimation is not affected by CFO and TO [11]. Then, BS can estimate the AoAs of incident signals accurately.

B. AoA Estimation and Spatial Filtering

1) *AoA Estimation:* We can stack all $M_s \times N_c$ CSI estimates (from N_c subcarriers and M_s packets) to obtain the matrix $\hat{\mathbf{H}}_C \in \mathbb{C}^{P_t Q_t \times N_c M_s}$, where the $[(m-1)N_c + n]$ th column of $\hat{\mathbf{H}}_C$ is $\hat{\mathbf{h}}_{C,n,m}$. Construct the correlation matrix as

$$\mathbf{R}_x = [\hat{\mathbf{H}}_C (\hat{\mathbf{H}}_C)^H] / (M_s N_c). \quad (5)$$

Note that $\hat{\mathbf{H}}_C (\hat{\mathbf{H}}_C)^H = \sum_{n,m}^{N_c, M_s} \hat{\mathbf{h}}_{C,n,m} (\hat{\mathbf{h}}_{C,n,m})^H$ does not contain $e^{j2\pi m T_s^p [f_{c,d,k} + \delta_f(m)]} e^{-j2\pi n \Delta f [\tau_{c,k} + \delta_\tau(m)]}$. Therefore, \mathbf{R}_x can combine the energy of all the symbols coherently. Here, we propose a refined 2D MUSIC method to estimate the 2D AoA based on \mathbf{R}_x .

Algorithm 1: 2D two-step Newton descent minimum searching method

Input: The range of φ : Φ_φ ; the range of θ : Φ_θ ; the number of grid points: N_i ; the maximum iteration round ind_{max} ; the MUSIC spectrum function: $f(\mathbf{p})$.

Output: Estimation results: $\Theta = \{\hat{\mathbf{p}}_k\}_{k \in \{0, \dots, N_s-1\}}$.

Initialize:

1) Φ_φ and Φ_θ are both divided evenly into $N_i - 1$ pieces with N_i grid points to generate grid $\hat{\Phi}_\varphi$ and $\hat{\Phi}_\theta$.

2) Set a null space Θ .

Process:

Step 1: **foreach** $\mathbf{p}_{i,j} \in \hat{\Phi}_\varphi \times \hat{\Phi}_\theta$ **do**

 Calculate the spatial spectrum as \mathbf{S} , where
 $[\mathbf{S}]_{i,j} = [f(\mathbf{p}_{i,j})]^{-1}$.

end

Step 2: Search the maximal values of \mathbf{S} to form the set $\bar{\Theta}_d$.

Step 3: Derive the Hessian matrix and the gradient vector of $f(\mathbf{p})$ as $\mathbf{H}_p(\mathbf{p})$ and $\nabla_p f(\mathbf{p})$, respectively.

Step 4: **foreach** $\mathbf{p}_{i,j} \in \bar{\Theta}_d$ **do**

$k=1$;
 $\mathbf{p}^{(0)} = \mathbf{p}_{i,j}$;
 $\mathbf{p}^{(k)} = \mathbf{p}^{(k-1)} - [\mathbf{H}_p(\mathbf{p}^{(k-1)})]^{-1} \nabla_p f(\mathbf{p}^{(k-1)})$;
 while $\|\mathbf{p}^{(k)} - \mathbf{p}^{(k-1)}\| > \varepsilon$ **and** $k \leq ind_{max}$ **do**
 $\mathbf{p}^{(k)} = \mathbf{p}^{(k-1)} - [\mathbf{H}_p(\mathbf{p}^{(k-1)})]^{-1} \nabla_p f(\mathbf{p}^{(k-1)})$;
 end
 $\mathbf{p}^{(k)}$ is put into output set Θ ;

end

By applying eigenvalue decomposition to \mathbf{R}_x , we obtain

$$[\mathbf{U}_x, \mathbf{\Sigma}_x] = \text{eig}(\mathbf{R}_x), \quad (6)$$

where $\text{eig}(\mathbf{M})$ represents the eigenvalue decomposition of \mathbf{M} , $\mathbf{\Sigma}_x$ is the real-value eigenvalue diagonal matrix in descending order, and \mathbf{U}_x is the orthogonal eigen matrix. The number of identifiable AoAs is denoted by N_A ¹, which can be estimated using the minimum description length (MDL) method [22]. The noise subspace of \mathbf{R}_x is $\mathbf{U}_N = [\mathbf{U}_x]_{:, N_A+1: P_t Q_t}$, and then we formulate the angle spectrum function as [23]

$$f_a(\mathbf{p}) = \mathbf{a}^H(\mathbf{p}) \mathbf{U}_N (\mathbf{U}_N)^H \mathbf{a}(\mathbf{p}), \quad (7)$$

where $\mathbf{a}(\mathbf{p})$ is given in (2). The angle spectrum is further obtained as [23]

$$S_a(\mathbf{p}) = [\mathbf{a}^H(\mathbf{p}) \mathbf{U}_N (\mathbf{U}_N)^H \mathbf{a}(\mathbf{p})]^{-1}. \quad (8)$$

The minimum points of $f_a(\mathbf{p})$, i.e., the maximum points of $S_a(\mathbf{p})$ correspond to the AoAs to be estimated. We propose a 2D two-step Newton descent method to derive the minimum points of $f_a(\mathbf{p})$, which is presented in **Algorithm 1**. The initial points for Newton descent iteration are given by a coarse-granularity grid search [15]. The 2D Newton descent

¹ $N_A \leq K$ since there may be targets with similar AoAs. The targets with similar AoA will be identified with different Doppler frequencies or ranges in the following subsections.

procedures, i.e., **Step 4**, are derived by setting the first-order derivative of the Taylor series of the spectrum function in (7) to be 0.

To identify the minimum of $f_a(\mathbf{p})$, we substitute $f(\mathbf{p})$, $\mathbf{H}_p(\mathbf{p})$, and $\nabla_p f(\mathbf{p})$ in **Algorithm 1** with (7), Hessian matrix and the gradient vector of $f_a(\mathbf{p})$, respectively. Note that **Algorithm 1** can also be used in the one-dimensional (1D) parameter estimation by treating the second parameter to be a constant value.

The AoAs of UE and scatterers are obtained with **Algorithm 1** as $\hat{\mathbf{p}}_{R,l}^U = (\hat{\varphi}_l, \hat{\theta}_l)$. The direction of UE (DoU) is set as $\hat{\mathbf{p}}_{R,0}^U = (\hat{\varphi}_0, \hat{\theta}_0)$, and will be identified in Section III-G by identifying the sensing result with the smallest range. Furthermore, based on the eigenvalue vector, denoted by $\mathbf{v}_s = \text{vec}(\Sigma_x)$, obtained in the MUSIC process, we can also estimate the variance of $\bar{\mathbf{n}}_{t,n,m}$ as $\hat{\sigma}_N^2$. According to [23], $\mathbf{v}_s \in \mathbb{C}^{P_t Q_t \times 1}$ can be expressed as

$$[\mathbf{v}_s]_i = \begin{cases} \sigma_{s,i}^2 + \sigma_N^2, & i \leq N_A \\ \sigma_N^2, & i > N_A \end{cases}, \quad (9)$$

where $\sigma_{s,i}^2$ is the power of the i th incident signal. Therefore, we obtain the estimation of the noise power as

$$\hat{\sigma}_N^2 = \sum_{i=N_A+1}^{P_t Q_t} [\mathbf{v}_s]_i / (P_t Q_t - N_A). \quad (10)$$

2) *Spatial Filtering*: In order to estimate the range of the UE and scatterers, we generate and apply a baseband spatial filter for each AoA estimate, i.e., receiving the signals in $\hat{\mathbf{p}}_{R,l}^U = (\hat{\varphi}_l, \hat{\theta}_l)$. The BF vector for receiving the signals from the l th AoA is generated with the LS method as $\mathbf{w}_{R,l} = \frac{[\mathbf{a}^T(\hat{\mathbf{p}}_{R,l}^U)]^\dagger}{\sqrt{\|[\mathbf{a}^T(\hat{\mathbf{p}}_{R,l}^U)]^\dagger\|_2^2}}$ [24], where $[\cdot]^\dagger$ represents the pseudo-inverse of a matrix. Let Θ_x^l be the index set of the targets in the l th AoA, where the number of elements of Θ_x^l is N_x^l . Using $\mathbf{w}_{R,l}$ to filter $\hat{\mathbf{h}}_{C,n,m}$, we obtain

$$\begin{aligned} \hat{\mathbf{h}}_{C,n,m}^l &= (\mathbf{w}_{R,l})^H \hat{\mathbf{h}}_{C,n,m} = h_{C,n,m}^l + \bar{\mathbf{n}}_{t,n,m}^l \\ &= \sum_{k \in \Theta_x^l} \left[e^{j2\pi m T_s^p \tilde{f}_{d,k,m}} e^{-j2\pi n \Delta f \tilde{\tau}_{k,m}} \right] + \bar{\mathbf{n}}_{t,n,m}^l, \end{aligned} \quad (11)$$

where $h_{C,n,m}^l$ is the actual channel response, $\tilde{f}_{d,k,m} = f_{d,k,m} + \delta_f(m)$, $\tilde{\tau}_{k,m} = \tau_{c,k} + \delta_\tau(m)$, and $\chi_{R,l,k} = (\mathbf{w}_{R,l})^H \mathbf{a}(\mathbf{p}_{R,k}^U)$ is the receive gain of the signals from the l th AoA. Moreover, the equivalent interference-plus-noise term is

$$\begin{aligned} \bar{\mathbf{n}}_{t,n,m}^l &= (\mathbf{w}_{R,l})^H \bar{\mathbf{n}}_{t,n,m} + \sum_{k=0,k \notin \Theta_x^l}^{K-1} \left[e^{j2\pi m T_s^p \tilde{f}_{d,k,m}} e^{-j2\pi n \Delta f \tilde{\tau}_{k,m}} \right] \\ &\quad \times \sqrt{P_t} b_{C,k} \chi_{T,k} \chi_{R,l,k}, \end{aligned} \quad (12)$$

where $\chi_{R,l,k} = (\mathbf{w}_{R,l})^H \mathbf{a}(\mathbf{p}_{R,k}^U)$ ($k \notin \Theta_x^l$) is the receive gain of interference. It is easy to see that $\|\chi_{R,l,k}\|_2^2 \ll \|\chi_{R,l,k}\|_2^2$.

After $\hat{\mathbf{h}}_{C,n,m}$ at N_c subcarriers of M_s packets are all filtered by the baseband beamformer, $\mathbf{w}_{R,l}$, we stack all the spatially filtered CSI to form $\hat{\mathbf{H}}_C^l$, where $[\hat{\mathbf{H}}_C^l]_{n,m} = \hat{\mathbf{h}}_{C,n,m}^l$. The actual CSI corresponding to $\hat{\mathbf{H}}_C^l$ shall be \mathbf{H}_C^l , where $[\mathbf{H}_C^l]_{n,m} = h_{C,n,m}^l$.

Algorithm 2: KF-based CSI Enhancer

Input: The observation variance $\sigma_N^2 = \hat{\sigma}_N^2$; The transfer factor $A = \hat{A}_{s,l}$; The observation sequence $\hat{\mathbf{h}}_C = [\hat{\mathbf{h}}_{C,n,m}^U]_{:,q}$.

Output: Filtered sequence $\bar{\mathbf{h}}_C = [\bar{\mathbf{h}}_{C,n,m}^U]_{:,q}$; The variance after KF filtering $\hat{\sigma}_{NK}^2$.

Step 1: The dimension of $\hat{\mathbf{h}}_C$ is obtained as M ;

Step 2: $[\bar{\mathbf{h}}_C]_0 = [\hat{\mathbf{h}}_C]_0$;

Step 3: $p_{w,0} = \sum_{p=0}^{P-1} \|[\hat{\mathbf{h}}_C]_p(A)^{-p} - [\hat{\mathbf{h}}_C]_0\|_2^2 / P$;

Step 4: for $p = 1$ **to** $M - 1$ **do**

$[\hat{\mathbf{h}}_C]_p^- = A[\bar{\mathbf{h}}_C]_{p-1}$;
 $p_{w,p}^- = A p_{w,p-1} A^*$;
 $K_p = (p_{w,p}^-)^* (p_{w,p}^- + \sigma_N^2)^{-1}$;
 $[\bar{\mathbf{h}}_C]_p = [\hat{\mathbf{h}}_C]_p^- + K_p([\hat{\mathbf{h}}_C]_p - [\hat{\mathbf{h}}_C]_p^-)$;
 $p_{w,p} = (1 - K_p) p_{w,p}^-$;

end

for $p = M - 1$ **to** 1 **do**

$[\hat{\mathbf{h}}_C]_{p-1}^- = A^{-1}[\bar{\mathbf{h}}_C]_p$;
 $p_{w,p-1}^- = A^{-1} p_{w,p} (A^{-1})^*$;
 $K_p = (p_{w,p-1}^-)^* (p_{w,p-1}^- + \sigma_N^2)^{-1}$;
 $[\bar{\mathbf{h}}_C]_{p-1} = [\hat{\mathbf{h}}_C]_{p-1}^- + K_p([\hat{\mathbf{h}}_C]_{p-1} - [\hat{\mathbf{h}}_C]_{p-1}^-)$;
 $p_{w,p-1} = (1 - K_p) p_{w,p-1}^-$;

end

return $\bar{\mathbf{h}}_C$; $\hat{\sigma}_{NK}^2 = p_{w,p-1}$.

C. DRDE Step 1: Decoupling Range and Doppler Estimation

We introduce a theorem to decouple the estimation of Doppler and delay (range), which also forms the basis for the DRDE method. Since $\hat{\mathbf{H}}_C^l$ has steering vector-like expressions, i.e., $e^{j2\pi m T_s^p \tilde{f}_{d,k,m}}$ and $e^{-j2\pi n \Delta f \tilde{\tau}_{k,m}}$, we can construct the range and Doppler steering vectors, respectively, as

$$\mathbf{a}_{r,k} = [e^{-j2\pi n \Delta f \tilde{\tau}_{k,m}}]_{n=0,1,\dots,N_c-1} \in \mathbb{C}^{N_c \times 1}, \quad (13)$$

$$\mathbf{a}_{f,k} = [e^{j2\pi m T_s^p \tilde{f}_{d,k,m}}]_{m=0,1,\dots,M_s-1} \in \mathbb{C}^{M_s \times 1}, \quad (14)$$

where $\tilde{r}_{k,m} = \tilde{\tau}_{k,m} \times c$.

Then, based on (11), $\hat{\mathbf{H}}_C^l$ can be rewritten as

$$\hat{\mathbf{H}}_C^l = \mathbf{a}_{r,k} S_k (\mathbf{a}_{f,k})^T + \mathbf{W}_{tr}^l, \quad (15)$$

where $S_k = \sqrt{P_t} b_{C,k} \chi_{R,k} \chi_{T,k}$, and $[\mathbf{W}_{tr}^l]_{n,m} = \bar{\mathbf{n}}_{t,n,m}^l$. We can use **Theorem 1** to decouple the estimation of range and Doppler.

Theorem 1. If $\bar{\mathbf{H}} = \mathbf{a}_r(r_l) S [\mathbf{a}_f(f_d)]^T + \mathbf{W} \in \mathbb{C}^{N_c \times M_s}$, where $\mathbf{a}_r(r) = [e^{-j2\pi n \Delta f \tilde{\tau}_c^r}]_{n=0,1,\dots,N_c-1} \in \mathbb{C}^{N_c \times 1}$, $\mathbf{a}_f(f_d) = [e^{j2\pi m T_s^p \tilde{f}_d}]_{m=0,1,\dots,M_s-1} \in \mathbb{C}^{M_s \times 1}$, S is irrelevant to \mathbf{a}_r and \mathbf{a}_f , and \mathbf{W} is a Gaussian noise matrix. Let the noise subspaces of $\bar{\mathbf{H}}$ and $\bar{\mathbf{H}}^T$ be $\mathbf{U}_{x,rN}$ and $\mathbf{U}_{x,fN}$, respectively. Then, the minimal values of $\|\mathbf{U}_{x,rN}^H \mathbf{a}_r(r)\|_2^2$ and $\|\mathbf{U}_{x,fN}^H \mathbf{a}_f(f)\|_2^2$ are $r = r_l$ and $f = f_d$, respectively.

Proof. The proof is provided in **Appendix A**. \square

Based on **Theorem 1**, the Doppler and range estimations are decoupled.

D. DRDE Step 2: DPO Estimation

Based on **Theorem 1**, we can use $\mathbf{R}_{X,f}^l = \frac{1}{N_c}(\hat{\mathbf{H}}_C^l)^T(\hat{\mathbf{H}}_C^l)^*$ to derive the noise subspace of $(\hat{\mathbf{H}}_C^l)^T$ to estimate the DPO. Here, $\mathbf{R}_{X,f}^l$ can be expressed as the average of the multiplication of the row vectors of $\hat{\mathbf{H}}_C^l$:

$$\mathbf{R}_{X,f}^l = \frac{1}{N_c} \sum_{n=1}^{N_c} \left([\hat{\mathbf{H}}_C^l]_{n,:} \right)^T \left([\hat{\mathbf{H}}_C^l]_{n,:} \right)^*, \quad (16)$$

where $[\hat{\mathbf{H}}_C^l]_{n,:}$ is the n th row of $\hat{\mathbf{H}}_C^l$. According to (11), given the same n , the terms containing $e^{-j2\pi n \Delta f \tilde{\tau}_{k,m}}$ will all be canceled. Therefore, there are only phase shift terms of DPO differences in $\mathbf{R}_{X,f}^l$, and the MUSIC-based method can generate Doppler frequency estimates approaching most DPOs of M_s packets.

By applying eigenvalue decomposition to $\mathbf{R}_{X,f}^l$, we obtain

$$[\mathbf{U}_{x,f}^l, \mathbf{\Sigma}_{x,f}^l] = \text{eig}(\mathbf{R}_{X,f}^l), \quad (17)$$

where $\mathbf{\Sigma}_{x,f}^l$ is the eigenvalue diagonal matrix, and $\mathbf{U}_{x,f}^l$ is the corresponding eigen matrix. The noise subspace of $\mathbf{U}_{x,fN}^l = [\mathbf{U}_{x,f}^l]_{:,N_{x,f}^l:M_s}$, where $N_{x,f}^l$ is the number of scatterers with different Doppler frequencies and similar AoAs, which can be obtained using the method in **Appendix B**.

According to **Theorem 1**, the Doppler spectrum function and Doppler spectrum are given, respectively, by

$$f_f(f) = \mathbf{a}_f(f)^H \mathbf{U}_{x,fN} (\mathbf{U}_{x,fN})^H \mathbf{a}_f(f), \quad (18)$$

$$S_f(f) = [\mathbf{a}_f(f)^H \mathbf{U}_{x,fN} (\mathbf{U}_{x,fN})^H \mathbf{a}_f(f)]^{-1}. \quad (19)$$

According to **Theorem 1**, the minimal point of $f_f(f)$, i.e., the maximal point of $S_f(f)$ is the Doppler estimation results. **Algorithm 1** can be used to identify the above minimal value by treating the second parameter, θ , in **Algorithm 1** as a discarded constant. Note that $f(\mathbf{p})$, $\nabla_{\mathbf{p}} f(\mathbf{p})$ and $\mathbf{H}_{\mathbf{p}}(\mathbf{p})$ in **Algorithm 1** are replaced by (18), $\frac{\partial f_f(f)}{\partial f}$, and $\frac{\partial^2 f_f(f)}{\partial^2 f}$ for Doppler estimation, respectively.

The estimated DPOs for the targets in the l th AoA are denoted by $\Theta_{n_f}^l = \left\{ \hat{f}_{d,n_f}^l \right\}_{n_f=0, \dots, N_{x,f}^l-1}$.

E. KF-based CSI Enhancer

With the spatially filtered outputs $\hat{\mathbf{H}}_C^l$ and the estimated DPO, we now introduce the KF-based CSI enhancer to suppress the TO terms.

We can rewrite (11) as

$$\begin{aligned} \hat{h}_{C,n,m}^l &= h_{C,n,m}^l + \bar{n}_{t,n,m}^l \\ &= \sum_{k \in \Theta_x^l} \left[A_k e^{j2\pi(mT_s \tilde{f}_{d,k,m} - n \Delta f \tau_{c,k})} e^{-j2\pi n \Delta f \delta \tau(m)} \right] + \bar{n}_{t,n,m}^l, \end{aligned} \quad (20)$$

where $A_k = \sqrt{P_t} b_{C,k} \chi_{T,k} \chi_{R,k}$, and Θ_x^l represents the index set of the targets in the l th AoA as shown in Section III-B2.

Then, we model the state transfer of the actual CSI, \mathbf{H}_C^l , in the m axis. Let $A_{s,\bar{k}} = e^{j2\pi T_s^p \tilde{f}_{d,\bar{k}}} (\bar{k} \in \Theta_x^l)$ be the state transfer factor, where $\tilde{f}_{d,\bar{k}} = E(\tilde{f}_{d,\bar{k},m})$, then we obtain

$$[\mathbf{H}_C^l]_{n,m+1} = [\mathbf{H}_C^l]_{n,m} A_{s,\bar{k}} + \Delta_h(m), \quad (21)$$

where $\Delta_h(m)$ is a time-varying noise term, and is expressed as

$$\Delta_h(m) \approx \left[A_{\bar{k}} e^{j2\pi[(m+1)T_s^p \tilde{f}_{d,\bar{k},m} - n \Delta f \tau_{c,\bar{k}}]} - (e^{-j2\pi n \Delta f \delta \tau(m+1)} - e^{-j2\pi n \Delta f \delta \tau(m)}) \right] + \bar{n}_{t,n,m}^l, \quad (22)$$

where $\bar{n}_{t,n,m}^l$ is the time-varying error term generated by the CSI terms with $k \neq \bar{k}$. Moreover, (22) is available when σ_f is not too large. Since CFO can be reduced to a small value according to [11], (22) can be satisfied.

Based on (21) and (22), there is a time-varying noise term, $\Delta_h(m)$ in \mathbf{H}_C^l , containing TO in the state transfer process. We introduce a KF to filter each row of \mathbf{H}_C^l to suppress the time-varying TO terms, exploiting the estimated DPO, \hat{f}_{d,n_f}^l , and $\hat{A}_{s,l} = e^{j2\pi T_s^p \hat{f}_{d,n_f}^l}$ as the prior information. Note that the KF can work with a tolerance of σ_f since (22) is available with a tolerance of σ_f , as will be validated in Section V.

However, we cannot use KF to filter each column of \mathbf{H}_C^l to suppress the CFO terms. This is because given a fixed m , $e^{j2\pi m T_s^p \delta f(m)}$ does not change with the variation of n . In this paper, we focus on the performance of TO suppression.

Let $\hat{\mathbf{h}}_C$ and $\bar{\mathbf{h}}_C$ denote a row of \mathbf{H}_C^l and its KF-filtered vector, respectively. The prior estimation of $[\hat{\mathbf{h}}_C]_p$ can be expressed as

$$[\hat{\mathbf{h}}_C]_p^- = [\hat{\mathbf{h}}_C]_{p-1} A, \text{ for } p \in \{1, \dots, M_s - 1\}, \quad (23)$$

where $A = \hat{A}_{s,l}$ for filtering. Then, $[\bar{\mathbf{h}}_C]_p$ can be further updated as [25]

$$[\bar{\mathbf{h}}_C]_p = [\hat{\mathbf{h}}_C]_p^- + K_p ([\hat{\mathbf{h}}_C]_p - [\hat{\mathbf{h}}_C]_p^-), \quad (24)$$

where K_p is the data fusion factor. Moreover, K_p is expressed as [25]

$$K_p = (p_{w,p}^-)^* (p_{w,p}^- + \sigma_N^2)^{-1}, \quad (25)$$

where σ_N^2 is the power of interference plus noise, and its estimation is $\hat{\sigma}_N^2$. Here, $p_{w,p}^-$ is the variance of the prior estimation, as given by [25]

$$p_{w,p}^- = A p_{w,p-1} A^*, \quad (26)$$

where $p_{w,p-1}$ is the variance of the last estimation and given by [25]

$$p_{w,p} = (1 - K_p) p_{w,p}^-. \quad (27)$$

Specifically, $p_{w,0}$ is the variance of the initial observation. According to (21) and (22), $p_{w,0}$ can be estimated as

$$p_{w,0} \approx \frac{1}{P} \sum_{p=0}^{P-1} \| [\hat{\mathbf{h}}_C]_p A^{-p} - [\hat{\mathbf{h}}_C]_0 \|^2. \quad (28)$$

Based on (23), (24), (25), (26), (27), and (28), we propose the KF-based CSI enhancer as shown in **Algorithm 2**. Note that we further add an inverse version of KF in **Step 4** to completely exploit the sensing information, where the transfer factor is updated as A^{-1} . By exploiting the estimated DPOs as the prior information, **Algorithm 2** can suppress the time-varying TO.

$$\begin{aligned}
x_n &= \begin{cases} \frac{b^2 c + \sqrt{b^4 c^2 + b^2(a^2 - c^2)(b^2 + a^2 \cot^2 \tilde{\theta}_l + a^2 \tan^2 \tilde{\varphi}_l + a^2 \cot^2 \tilde{\theta}_l \tan^2 \tilde{\varphi}_l)}}{b^2 + a^2 \cot^2 \tilde{\theta}_l + a^2 \tan^2 \tilde{\varphi}_l + a^2 \cot^2 \tilde{\theta}_l \tan^2 \tilde{\varphi}_l}, & \text{for } \cos(\tilde{\varphi}_l) \geq 0, \\ \frac{b^2 c - \sqrt{b^4 c^2 + b^2(a^2 - c^2)(b^2 + a^2 \cot^2 \tilde{\theta}_l + a^2 \tan^2 \tilde{\varphi}_l + a^2 \cot^2 \tilde{\theta}_l \tan^2 \tilde{\varphi}_l)}}{b^2 + a^2 \cot^2 \tilde{\theta}_l + a^2 \tan^2 \tilde{\varphi}_l + a^2 \cot^2 \tilde{\theta}_l \tan^2 \tilde{\varphi}_l}, & \text{for } \cos(\tilde{\varphi}_l) < 0, \end{cases} \\
y_n &= x_n \tan \tilde{\varphi}_l, \\
z_n &= \sqrt{(x_n^2 + y_n^2) \left(1 + \frac{1}{\tan^2 \tilde{\theta}_l}\right)} \cos(\tilde{\theta}_l).
\end{aligned} \tag{33}$$

F. DRDE Step 3: Range Estimation

For the scatterers with the l th AoA and n_f th Doppler, the state transfer factor is $\hat{A}_{s,n_f}^l = e^{j2\pi T_s^p \hat{f}_{d,n_f}^l}$ according to Section III-E. We use **Algorithm 2** to filter all N_c rows of $\hat{\mathbf{H}}_C$ by replacing the input with $A = \hat{A}_{s,n_f}^l = e^{j2\pi T_s^p \hat{f}_{d,n_f}^l}$ and $\hat{\mathbf{h}}_C = [\hat{\mathbf{H}}_C]_{n,:}$, and the filtered CSI is denoted by $\hat{\mathbf{H}}_{C,n_f}^{l,(1)}$.

According to **Theorem 1**, the range can then be estimated based on $\mathbf{R}_{X,r}^{l,n_f} = \frac{1}{M_s} \hat{\mathbf{H}}_{C,n_f}^{l,(1)} (\hat{\mathbf{H}}_{C,n_f}^{l,(1)})^H$. The eigenvalue decomposition of $\mathbf{R}_{X,r}^{l,n_f}$ is

$$[\mathbf{U}_{x,r}^{l,n_f}, \boldsymbol{\Sigma}_{x,r}^{l,n_f}] = \text{eig}(\mathbf{R}_{X,r}^{l,n_f}), \tag{29}$$

where $\boldsymbol{\Sigma}_{x,r}^{l,n_f}$ is the eigenvalue diagonal matrix, and $\mathbf{U}_{x,r}^{l,n_f}$ is the corresponding eigen matrix. The noise subspace of $\mathbf{R}_{X,r}^{l,n_f}$ is $\mathbf{U}_{x,rN}^{l,n_f} = [\mathbf{U}_{x,r}^{l,n_f}]_{:,N_{x,r}^{l,n_f}:N_c}$, where $N_{x,r}^{l,n_f}$ is the number of scatterers with different ranges, which can also be determined using the method in **Appendix B**.

Based on **Theorem 1**, the range spectrum function and range spectrum are given, respectively, by

$$f_r(r) = \mathbf{a}_r(r)^H \mathbf{U}_{x,rN} (\mathbf{U}_{x,rN})^H \mathbf{a}_r(r), \tag{30}$$

$$S_r(r) = [\mathbf{a}_r(r)^H \mathbf{U}_{x,rN} (\mathbf{U}_{x,rN})^H \mathbf{a}_r(r)]^{-1}. \tag{31}$$

The minimal point of $f_r(r)$, i.e., the maximal point of $S_r(r)$ corresponds to the range to be estimated. **Algorithm 1** can be used to identify the above minimal value. Note that $f(\mathbf{p})$, $\nabla_{\mathbf{p}} f(\mathbf{p})$ and $\mathbf{H}_{\mathbf{p}}(\mathbf{p})$ in **Algorithm 1** are replaced by (30), $\frac{\partial f_r(r)}{\partial r}$, and $\frac{\partial^2 f_r(r)}{\partial^2 r}$ for range estimation, respectively.

The estimated aggregate range for the targets with the l th AoA and n_f th Doppler frequency is denoted by $\Theta_{n_f,r}^l = \left\{ \hat{r}_{n_f,n_r}^l \right\}_{n_r=0, \dots, N_{x,r}^{l,n_f}}$. Note that $l = 0$ is for the range of UE.

The location of a target is not related to the Doppler frequency and only related to the AoA and range, and the range estimation method can only sense the targets in the specified l th AoA. Therefore, the range estimates are naturally matched with the AoA estimates and do not need to match the DPO estimates.

G. UL Bi-static JCAS Localization Method

In this subsection, we estimate the locations of the UE and scatterers based on the estimated AoAs and ranges obtained in Section III-B and Section III-F.

After \hat{r}_{n_f,n_r}^l for all $l \in \{0, \dots, N_A - 1\}$, $n_f \in \{0, \dots, N_{x,f}^l - 1\}$, and $n_r \in \{0, \dots, N_{x,r}^{l,n_f} - 1\}$ are estimated, the AoA and range pair for an estimated target can be

combined as $\Phi_{n_f,n_r}^l = \{\hat{\mathbf{p}}_{R,l}^U, \hat{r}_{n_f,n_r}^l\}$. When the SNR is high enough, the total number of estimates is K .

To identify the AoA and range estimates for UE, we exploit the fact that the UE's range shall be the smallest among all the range estimates. Let $\{\hat{\mathbf{p}}_{R,0}^U, \hat{r}_{n_f,n_0}^0\}$ denote the identified AoA and range of UE, where \hat{r}_{n_f,n_0}^0 is the smallest range estimate.

In the global coordinate system centered at BS, the location of the UE is

$$\boldsymbol{\Omega}_0 = (\hat{r}_{n_f,n_0}^0 \sin \hat{\theta}_0 \cos \hat{\varphi}_0, \hat{r}_{n_f,n_0}^0 \sin \hat{\theta}_0 \sin \hat{\varphi}_0, \hat{r}_{n_f,n_0}^0 \cos \hat{\theta}_0). \tag{32}$$

Construct a local coordinate system centered at BS by setting the direction from BS to UE as the positive direction of the x -axis. Then, the rotation angle from the global coordinate to the local coordinate is $\mathbf{p}_{rot} = (0^\circ, 90^\circ) - \hat{\mathbf{p}}_{R,0}^U$, and the l th AoA in the local coordinate is $\tilde{\mathbf{p}}_{R,l}^U = \hat{\mathbf{p}}_{R,l}^U + \mathbf{p}_{rot}$. We use $\boldsymbol{\Omega}_n^S = (x_n, y_n, z_n)$ to denote the location of the n th ($n = 0, \dots, K-1$) scatterer in the local coordinate. If the AoA and aggregate range of the n th scatterer is $\Phi_n = \{\tilde{\mathbf{p}}_{R,l}^U, \hat{r}_{n_f,n_r}^l\}$, we can obtain x_n , y_n and z_n as detailed in **Appendix D**. The results are provided in (33), where $a = \frac{\hat{r}_{n_f,n_r}^l}{2}$, $c = \frac{r_{n_f,n_0}^0}{2}$, and $b^2 = a^2 - c^2$.

We can finally rotate $\boldsymbol{\Omega}_n^S = (x_n, y_n, z_n)$ into the global coordinate by rotating the angle of $-\mathbf{p}_{rot}$ to obtain the location of the scatterer in the global coordinate system.

IV. PERFORMANCE ANALYSIS OF THE PROPOSED SENSING SCHEME

In this section, we analyze the Cramer-Rao bound (CRB) for the KF-based range estimation method and the complexity of the KF-based sensing scheme.

A. CRB for KF-based Range Estimation

The ranges of the UE or scatterers are derived using $\hat{h}_{C,n,m}^l$. Based on (20), the ideal signal for estimating the k th target is

$$\begin{aligned}
\hat{h}_{C,n,m}^l &= B_{n,m,k} + \bar{n}_{t,n,m}^l \\
&= \left[e^{j2\pi m T_s^p \hat{f}_{d,k,m}} e^{-j2\pi n \Delta f \frac{r_k}{c}} A_k \right] + \bar{n}_{t,n,m}^l,
\end{aligned} \tag{34}$$

where $A_k = \sqrt{P_t^U} \chi_{T,k} \chi_{R,k} b_{C,k}$. Since $\|\mathbf{w}_{R,l}\|_2 = 1$, $\bar{n}_{t,n,m}^l = (\mathbf{w}_{R,l})^H \mathbf{n}_{t,n,m}^l$ follows $\mathcal{CN}(0, \sigma_N^2)$. Therefore, $\hat{h}_{C,n,m}^l$ follows a Gaussian distribution with mean value $B_{n,m,k} = \sqrt{P_t^U} A_k e^{j2\pi m T_s^p \hat{f}_{d,k,m}} e^{-j2\pi n \Delta f \frac{r_k}{c}}$ and variance

σ_N^2 . The probability density function (PDF) of $\hat{h}_{C,n,m}^l$ can be expressed as

$$p_{\hat{h}_{C,n,m}^l}(h) = \frac{1}{\pi\sigma_N^2} e^{-\frac{1}{\sigma_N^2} \left| h - \sqrt{P_t^U} A_k e^{j2\pi m T_s^P \tilde{f}_{d,k,m}} e^{-j2\pi n \Delta f \frac{r_k}{c}} \right|^2}. \quad (35)$$

Further, since M_s OFDM symbols at N_c subcarriers are used, the PDF of all the used symbols is

$$p_{\mathbf{h}}(\mathbf{h}) = \frac{1}{(\pi\sigma_N^2)^{N_c M_s}} e^{-\frac{1}{\sigma_N^2} \sum_{n,m}^{N_c M_s} |h_{n,m} - B_{n,m,k}|^2}. \quad (36)$$

To obtain the CRB for the range estimation of r_k , we need to calculate $E \left\{ \frac{\partial^2 \ln p_{\mathbf{h}}(\mathbf{h})}{\partial^2 r_k} \right\}$. As detailed in **Appendix C**, we obtain

$$E \left\{ \frac{\partial^2 \ln p_{\mathbf{h}}(\mathbf{h})}{\partial^2 r_k} \right\} = -\gamma_k 8\pi^2 \Delta f^2 \frac{1}{c^2} M_s \sum_{n=0}^{N_c-1} n^2, \quad (37)$$

where $\gamma_k = \frac{P_t^U |A_k|^2}{\sigma_N^2}$ is the received SNR.

Finally, we can obtain the CRB for the range estimation as [26]

$$C_{r_k} = -E^{-1} \left\{ \frac{\partial^2 \ln p_{\mathbf{h}}(\mathbf{h})}{\partial^2 r_k} \right\} = \frac{c^2}{\gamma_k 8\pi^2 \Delta f^2 M_s \sum_{n=0}^{N_c-1} n^2}. \quad (38)$$

B. Complexity of the KF-based Sensing Scheme

The KF-based sensing scheme contains three MUSIC procedures to estimate AoA, Doppler, and range, respectively, and a KF filtering procedure for enhancing the CSI.

The major complexity of the MUSIC procedures is from the eigenvalue decomposition and is thus $\mathcal{O}(N_{MUSIC}^3)$, where $N_{MUSIC} = \max(P_t Q_t, N_c, M_s)$. The KF filtering procedure only needs to add two rounds of scalar multiplications over M_s CSI measurements at N_c subcarriers in parallel. Therefore, the complexity of the KF filtering procedure is $\mathcal{O}(M_s)$.

In conclusion, the complexity of the proposed KF-based sensing scheme is $\mathcal{O}(3N_{MUSIC}^3 + M_s)$, which is approximately $\mathcal{O}(N_{MUSIC}^3)$.

V. SIMULATION RESULTS

In this section, we present the simulation results for the range and location estimation root-MSEs (RMSEs) of the proposed KF-based JCAS processing scheme. The global simulation parameters are listed as follows.

A. System Setting

The carrier frequency is set to 28 GHz, the antenna interval, d_a , is half of the wavelength, the sizes of antenna arrays of the BS and user are $P_t \times Q_t = 8 \times 8$ and $P_r \times Q_r = 1 \times 1$, respectively. The subcarrier interval of UL preamble signal is $\Delta f = 480$ kHz, the subcarrier number is $N_c = 256$, and the bandwidth for JCAS is $B = N_c \Delta f = 122.88$ MHz. The number of OFDM packets is set to $M_s = 64$, the number of OFDM symbols of each packet (there is only one preamble OFDM symbol for CSI estimation in each packet) is $P_s =$

7 [27], and the time duration of each OFDM packet is thus $T_s^p = P_s / \Delta f = 14.58 \mu s$. The variance of the Gaussian noise is $\sigma_N^2 = kFTB = 4.9177 \times 10^{-12}$ W, where $k = 1.38 \times 10^{-23}$ J/K is the Boltzmann constant, $F = 10$ is the noise factor, and $T = 290$ K is the standard temperature. The locations of BS and UE are (50, 4.75, 7) m and (140, 0, 2) m, respectively. The location of the dumb scatterer is (60, 3, 3) m. Moreover, we set the reflection factor of the scatterer as $\sigma_{C\beta,k}^2 = 10$. The velocity of UE is (-40, 0, 0) km/h, and the velocities of BS and the dumb scatterers are (0, 0, 0) m/s.

Based on the above locations and velocities of BS, user, and scatterers, the AoAs, AoDs, ranges, and Doppler shifts between UE and BS, and between the scatterers and BS can be derived to generate UL channel response matrix according to the models proposed in Section II-C. Further, BS can use the KF-based JCAS processing scheme to estimate the ranges and locations of UE and dumb scatterers according to Section III. Communication SNR is defined as the SNR of each antenna element of BS. According to (4), the UL communication SNR is expressed as

$$\gamma_c = \frac{P_t^U \sum_{k=0}^{K-1} |b_{C,k} \chi_{T,k}|^2}{\sigma_N^2}. \quad (39)$$

The range and location estimation MSEs are defined as the mean values of all the square errors of the range and location estimation results under a certain set of simulation parameters. The RMSE is the square root of the MSE.

B. Sensing Performance

In this subsection, we present the sensing RMSEs of the proposed KF-based JCAS sensing scheme. We predefine two cases for comparison to show the TO suppression ability of the proposed KF-based JCAS processing scheme:

Case 1: The ranges of UE and scatterers are estimated by using the KF-based CSI enhancer and the DRDE method.

Case 2: The ranges of UE and scatterers are estimated by merely using the DRDE method without using the KF-based CSI enhancement.

Figs. 3(a) and 3(b) present the RMSEs of the AoA estimations of the scatterer and UE, respectively, under various σ_τ , σ_f and receiver array sizes. Figs. 3(a) and 3(b) show that the AoA estimation RMSEs are not affected by CFO and TO, and are influenced significantly by the receive array size. As the receive array size becomes larger, the AoA estimation RMSEs decrease due to more accumulated energy for sensing.

Fig. 4 shows the UE and scatterer's range and location estimation RMSEs of *cases 1* and *2*, under various σ_τ , using 8×8 receiver array when $\sigma_f = 240$ Hz.

Figs. 4(a) and 4(c) present the RMSEs of the scatterer and UE's range estimation RMSEs and the square roots of CRBs. Both the UE and scatterer range estimation RMSEs of *case 1* are smaller than those of *case 2* under the same SNR and $\sigma_\tau = 5$ ns. This is because the proposed KF-based method can suppress the noise and interference better as elaborated in Section III. When $\sigma_\tau = 0$ ns, i.e., there is no TO affecting range estimation, both the UE and scatterer range estimation

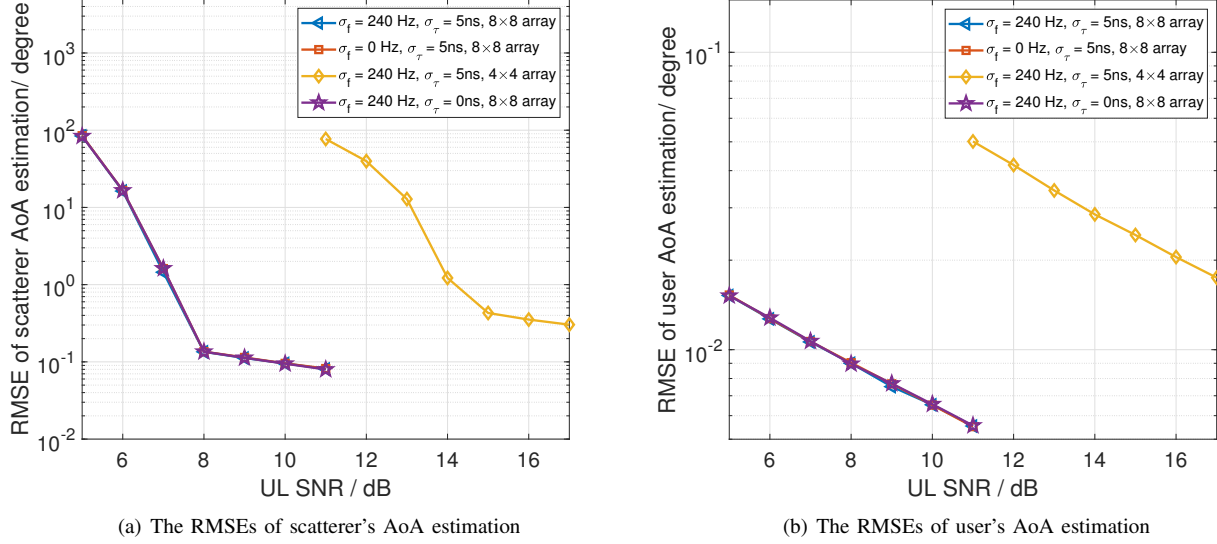


Fig. 3: The RMSEs of user and scatterer's AoAs estimation under various σ_τ , receiver array sizes and σ_f .

RMSEs of *cases* 1 and 2 approach the square roots of their CRBs. When $\sigma_\tau = 5$ ns, the proposed KF-based JCAS sensing method can still work at an acceptable RMSE level, while *case 2* cannot keep a satisfactory range estimation RMSE. From Fig. 4(a), we can see that the RMSE results of scatterer range estimation have two stages. In the low SNR regime, the AoA estimation RMSE is large according to Fig. 3(a), which makes the spatial filter cannot separate the CSI with different AoAs well, the scatterer range estimation RMSE is thus relatively high due to the low SNR and poor spatial filter performance. When SNR is larger than 7 dB, the AoA estimation is much more accurate, and the RMSE of scatterer range estimation also becomes a small and steadily decreasing value. As for the UE range estimation shown in Fig. 4(c), since the AoA estimation of UE is highly accurate in this SNR range according to Fig. 3(b), and the gain of LoS path is considerably larger than the NLoS path, the UE range estimation RMSEs are thus small and steady values. The gaps between the RMSEs of *case 1* and *case 2* under the same $\sigma_\tau > 0$ show the influence of the TO on the range estimation and the TO suppression ability of *case 1*.

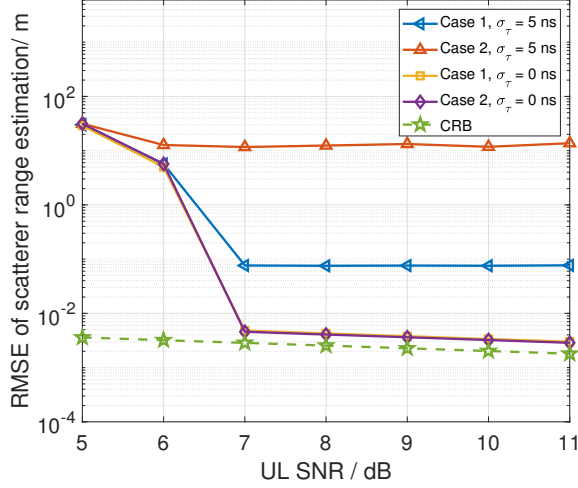
Figs. 4(b) and 4(d) present the RMSEs of the UE and scatterer's location estimation, respectively. From Fig. 4(d), we can see that the UE localization RMSEs of *cases* 1 and 2 are similar when $\sigma_\tau = 0$ ns, since the UE range estimation RMSEs and AoA estimation RMSEs of two cases are approximate according to Figs. 4(c) and 3(b). When $\sigma_\tau = 5$ ns, the UE localization RMSE of *case 1* is significantly smaller than that of *case 2*, since the KF-based CSI enhancer of *case 1* can suppress the TO better than *case 2* as shown in Fig. 4(c). As for the scatterer localization RMSEs shown in Fig. 4(b), the scatterer localization RMSEs of *case 1* under $\sigma_\tau = 0$ and 5 ns, and *case 2* under $\sigma_\tau = 0$ ns, are approximate. This is because the scatterer localization accuracy is determined by the scatterer's AoA and range estimation accuracy and

the UE localization accuracy. Specifically, there is an error proportional to $r \times \Delta\theta$, where r is the actual range and $\Delta\theta$ is the AoA error. When the range RMSE is lower than a certain small value, the AoA error is the main factor that determines the localization RMSE. When σ_τ is 5 ns, *case 2* can no longer keep satisfactory scatterer and UE localization RMSEs since the UE and scatterer range estimation RMSEs of *case 2* are both considerably large. In contrast, *case 1* can still achieve acceptable localization RMSEs because the range estimation RMSEs of *case 1* are still small. The minimum scatterer localization RMSE of *case 1* is about 20 dB lower than that of *case 2* in the large SNR regime.

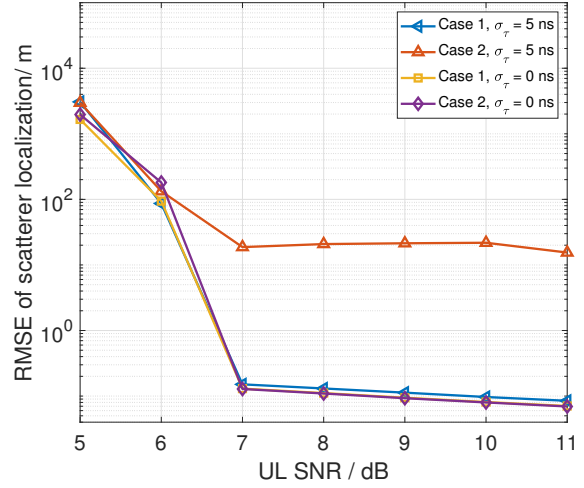
Fig. 5 shows the UE and scatterer's range and location estimation RMSEs of *cases* 1 and 2 using 4×4 and 8×8 receive arrays when $\sigma_\tau = 5$ ns and $\sigma_f = 240$ Hz.

Figs. 5(a) and 5(c) plot the UE and scatterer's range estimation RMSEs. Due to the noise and TO suppression abilities of the proposed KF-based CSI enhancer, the UE and scatterer's range estimation RMSEs of *case 1* are both smaller than those of *case 2*. Moreover, as the receive array size decreases from 8×8 to 4×4 , the SNR required to achieve the same range estimation RMSE increases by about 6 dB. This is because the larger the array is, the more energy is accumulated for sensing. The change in array size does not influence the minimum RMSE, which shows that it only changes the processing SNR and does not have significant impact on the range estimation performance bound of the proposed method.

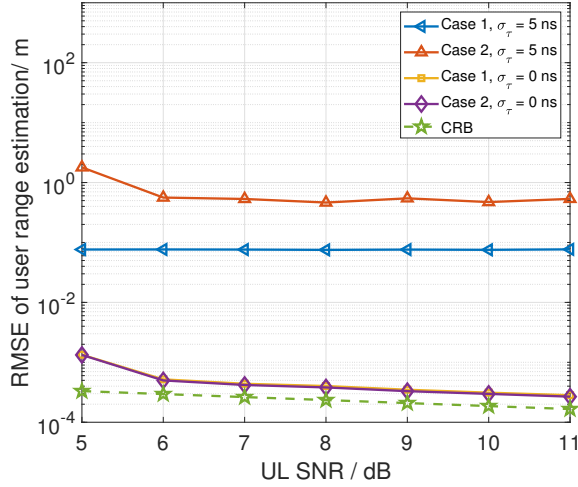
Figs. 5(b) and 5(d) present the UE and scatterer's localization RMSEs, respectively. The UE and scatterer's localization RMSEs of *case 1* are both smaller than those of *case 2* since the KF-based CSI enhancer suppresses the noise and TO. As the receive array size decreases from 8×8 to 4×4 , the SNR required to achieve the same localization RMSE increases by about 7 dB. It can be seen that the SNR gap of the localization RMSEs using 8×8 and 4×4 arrays is about 1 dB larger



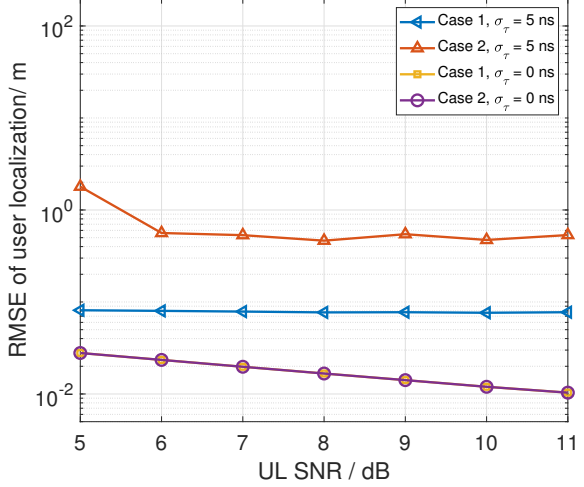
(a) The RMSEs of scatterer range estimation



(b) The RMSEs of scatterer localization



(c) The RMSEs of user range estimation



(d) The RMSEs of user localization

Fig. 4: The RMSEs of range estimation and localization of *cases* 1 and 2 under various σ_τ , using 8×8 receiver array when $\sigma_f = 240$ Hz.

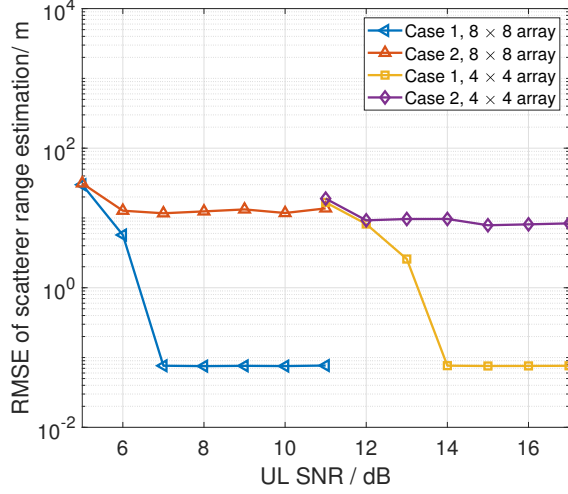
than that of the range estimation RMSE. This is because the AoA estimation accuracy also deteriorates as the array size decreases.

Fig. 6 shows the UE and scatterer's range and location estimation RMSEs of *case* 1 changing with σ_τ from 0 ns to 10 ns, when SNR is 8 dB, $\sigma_f = 100$ Hz, and using 8×8 receive array.

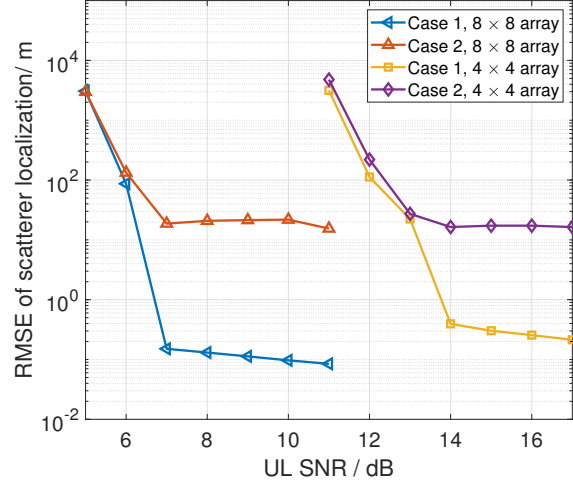
Fig. 6(a) plots the UE and scatterer's range estimation RMSEs, respectively. When $\sigma_\tau = 0$ ns, the UE range estimation RMSE is smaller than the scatterer range estimation RMSE, since the gain of the LoS path is larger than that of the NLoS path. As σ_τ increases, the TO becomes the main factor that affects the range estimation RMSE. Therefore, the UE and scatterer range estimation RMSEs approach to a similar value restricted by the TO suppression ability of the KF-based CSI enhancer.

Fig. 6(b) plots the UE and scatterer's localization RMSEs, respectively. The UE localization RMSE increases with the increase of σ_τ . This is because the accuracy of UE localization is affected by AoA and range estimation accuracy, and the AoA estimation RMSE is steady and small when SNR is 8 dB according to Fig. 3. After the range error dominates the localization error, the UE localization RMSE increases proportionally to the range estimation RMSE. In contrast, the scatterer localization accuracy is influenced by the AoA, scatterer range, and UE location estimation errors. Therefore, the scatterer localization RMSE is larger than the UE localization RMSE, and non-linearly increases with the increase of the σ_τ .

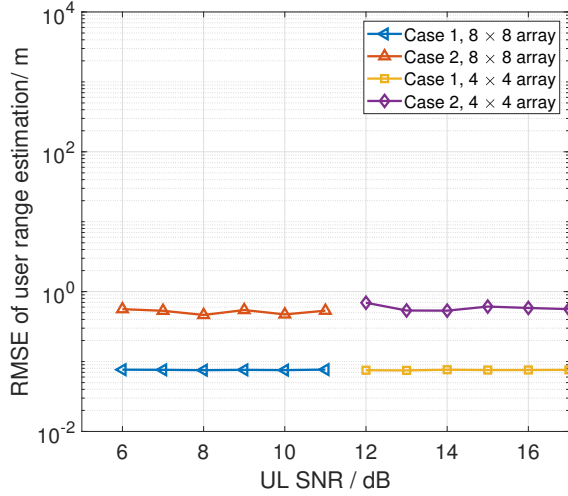
Fig. 7 shows the UE and scatterer's range and location estimation RMSEs of *case* 1 changing with σ_f from 0 Hz to 2000 Hz, when SNR is 8 dB, $\sigma_\tau = 5$ ns, and using 8×8 receive array.



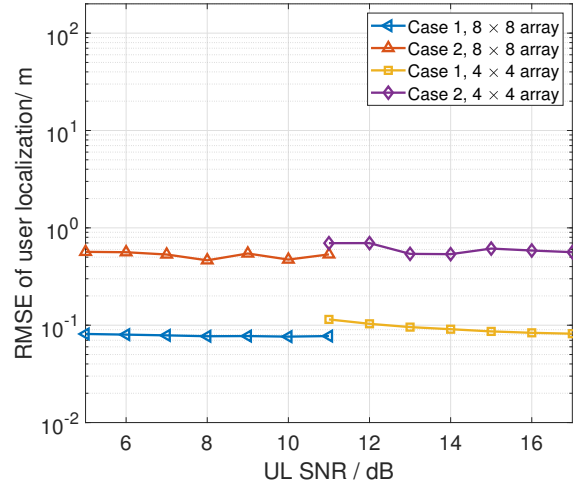
(a) The RMSEs of scatterer range estimation



(b) The RMSEs of scatterer localization



(c) The RMSEs of user range estimation



(d) The RMSEs of user localization

Fig. 5: The RMSEs of range estimation and localization of *cases* 1 and 2 using 4×4 and 8×8 receive arrays, when $\sigma_\tau = 5$ ns and $\sigma_f = 240$ Hz.

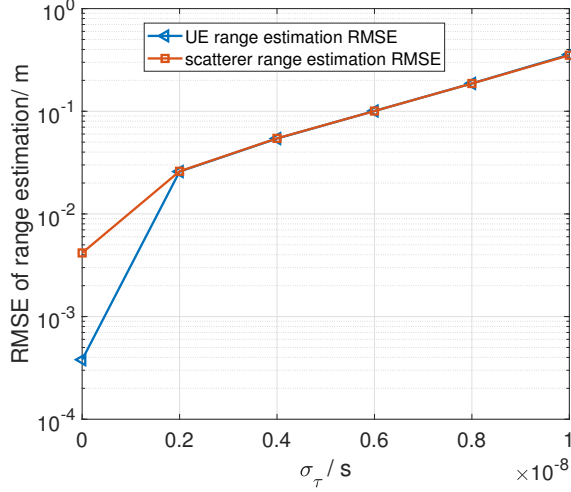
Fig. 7(a) plots the UE and scatterer's range estimation RMSEs. The UE and scatterer range estimation RMSEs approach each other and increase slowly as σ_f increases. This is partially due to the decoupled MUSIC-based range and Doppler estimations, which makes the change of σ_f not have great impact on range estimation. More importantly, the proposed KF-based CSI enhancer just needs the approximate estimation of DPOs to filter the CSI, as elaborated in Section III-E. Fig. 7(a) shows that the proposed KF-based CSI enhancer has considerable robustness in range estimation accuracy for the inaccurate estimation of DPOs.

Fig. 7(b) plots the UE and scatterer's localization RMSEs. As σ_f increases, the UE localization RMSE increases slightly and is almost the same as the UE range estimation RMSE according to Fig. 7(a). This is because the UE localization accuracy is determined by the AoA and range estimation accuracy, and the AoA estimation RMSE of UE is quite

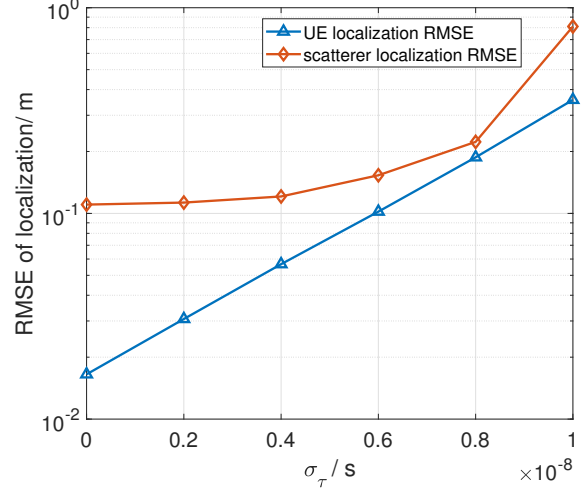
small when SNR is 8 dB according to Fig. 3(b). On the other hand, the scatterer localization RMSE increases more than that of the UE localization as σ_f increases. This is because the scatterer localization RMSE is influenced by the UE localization RMSE in addition to the scatterer's range and AoA estimation RMSEs. Moreover, the scatterer AoA estimation RMSE is larger than that of the UE AoA estimation according to Fig. 3. Thus, the scatterer localization RMSE is larger than the UE localization RMSE.

VI. CONCLUSION

In this paper, we propose a KF-based UL JCAS sensing scheme that can accurately estimate the ranges and locations of UE and dumb scatterers in the presence of clock asynchronism between UE and BS. Unlike the existing solutions, our scheme works without knowing the location of UE in advance. We first estimate the AoAs of incident signals and use them to form a

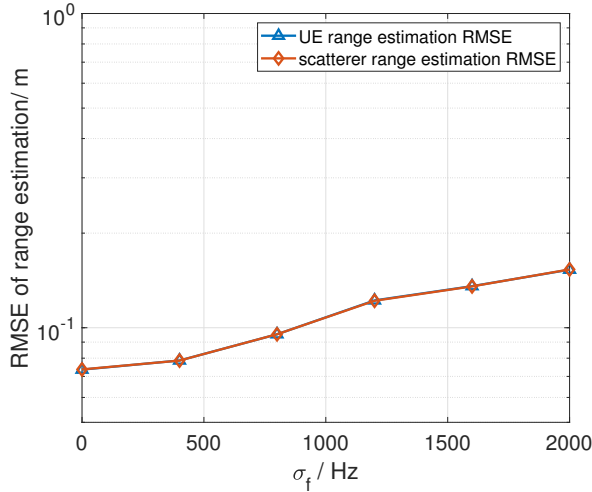


(a) The RMSEs of range estimation

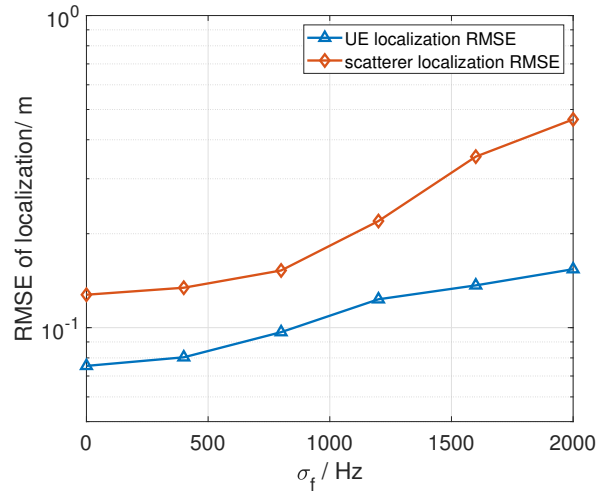


(b) The RMSEs of localization

Fig. 6: The RMSEs of range estimation and localization of the proposed KF-based JCAS processing method changing with σ_τ , when SNR is 8 dB, $\sigma_f = 100$ Hz and using 8×8 receive array.



(a) The RMSEs of range estimation



(b) The RMSEs of localization

Fig. 7: The RMSEs of range estimation and localization of the proposed KF-based JCAS processing method changing with σ_f , when SNR is 8 dB, $\sigma_\tau = 5$ ns and using 8×8 receive array.

spatial filter to separate the CSIs with different AoAs. Then, we use the DRDE method to estimate DPOs from the spatially filtered CSIs. Subsequently, we use the KF to suppress the time-varying noise-like TO in CSIs by exploiting the estimated DPOs as the prior information. Then, the ranges of UE and scatterers are accurately estimated with the DRDE method. Moreover, the range of UE is identified as the smallest one among all the range estimates. Finally, we propose the UL bi-static JCAS localization method to accurately locate the UE and dumb scatterers by utilizing the accurately estimated ranges and AoAs. Simulation results show that the localization RMSE of the proposed KF-based UL JCAS scheme is about 20 dB lower than the method without the KF-based CSI enhancer.

APPENDIX A PROOF OF THEOREM 1

Since \mathbf{W} is Gaussian noise matrix, we assume that $E\{\mathbf{W}\mathbf{W}^H\} = \sigma_W^2 \mathbf{I}_{N_c}$ and $E\{\mathbf{W}^H\mathbf{W}\} = \sigma_W^2 \mathbf{I}_{M_s}$. The autocorrelation of $\bar{\mathbf{H}}$ is

$$\begin{aligned} \mathbf{R}_{\mathbf{X},r} &= \frac{1}{M_s} E\{\bar{\mathbf{H}}[\bar{\mathbf{H}}]^H\} \\ &= S(S)^* \mathbf{a}_r(\mathbf{a}_f)^T (\mathbf{a}_f)^* (\mathbf{a}_r)^H + \sigma_W^2 \mathbf{I}_{N_c} \end{aligned} \quad (40)$$

By applying eigenvalue decomposition to $\mathbf{R}_{\mathbf{X},r}$, we obtain

$$[\mathbf{U}_{x,r}, \mathbf{\Sigma}_{x,r}] = \text{eig}(\mathbf{R}_{\mathbf{X},r}), \quad (41)$$

where $\mathbf{\Sigma}_{x,r}$ is the real-value diagonal eigenvalue matrix, $\mathbf{U}_{x,r}$ is the corresponding eigen matrix. Moreover, $\mathbf{U}_{x,r}$ can be

divided as $\mathbf{U}_{x,r} = [\mathbf{S}_{x,r}, \mathbf{U}_{x,rN}]$, where $\mathbf{U}_{x,rN}$ is the noise subspace. Because $\mathbf{U}_{x,rN}$ is an orthogonal unitary matrix, there are $[\mathbf{S}_{x,r}]^H \mathbf{U}_{x,rN} = \mathbf{0}$ and $[\mathbf{U}_{x,rN}]^H \mathbf{U}_{x,rN} = \mathbf{I}$, then we have

$$\mathbf{R}_{\mathbf{X},r} \mathbf{U}_{x,rN} = \mathbf{U}_{x,rN} \boldsymbol{\Sigma}_{x,r} = \sigma_W^2 \mathbf{U}_{x,rN}. \quad (42)$$

On the other hand, according to (40), we have

$$\begin{aligned} \mathbf{R}_{\mathbf{X},r} \mathbf{U}_{x,rN} &= S(S)^* \mathbf{a}_r (\mathbf{a}_f)^T (\mathbf{a}_f)^* (\mathbf{a}_r)^H \mathbf{U}_{x,rN} \\ &\quad + \sigma_W^2 \mathbf{U}_{x,rN}. \end{aligned} \quad (43)$$

By comparing (43) and (42), we have

$$S(S)^* \mathbf{a}_r (\mathbf{a}_f)^T (\mathbf{a}_f)^* (\mathbf{a}_r)^H \mathbf{U}_{x,rN} = \mathbf{0}, \quad (44)$$

where $(\mathbf{a}_f)^T (\mathbf{a}_f)^*$ is full-rank. Therefore, $[\mathbf{U}_{x,rN}]^H \mathbf{a}_r(r_l) = \mathbf{0}$. Thus, the minimal value of $\|\mathbf{U}_{x,rN}^H \mathbf{a}_r(r)\|_2^2$ is $r = r_l$. Similarly, we obtain the minimal value of $\|\mathbf{U}_{x,fN}^H \mathbf{a}_f(f)\|_2^2$ as $f = f_{d,l}$. This concludes the proof of **Theorem 1**.

APPENDIX B

DERIVATION OF $N_{x,f}^{l,n_f}$ OR $N_{x,r}^{l,n_r}$

First, we obtain the eigenvalue vector as $\mathbf{v}_x = \text{vec}(\boldsymbol{\Sigma}_x)$, where $\boldsymbol{\Sigma}_x = \boldsymbol{\Sigma}_{x,f}^{l,n_f}$ or $\boldsymbol{\Sigma}_{x,r}^{l,n_r}$ for Doppler frequency and range estimation, respectively. Let N denote the dimension of \mathbf{v}_x .

According to [23], \mathbf{v}_x can be expressed as

$$[\mathbf{v}_s]_i = \begin{cases} \sigma_{s,i}^2 + \sigma_N^2, & i \leq N_x \\ \sigma_N^2, & i > N_x \end{cases}, \quad (45)$$

where $N_x = N_{x,f}^{l,n_f}$ or $N_{x,r}^{l,n_r}$ for Doppler frequency and range estimation, respectively; and $\sigma_{s,i}^2$ is the power of the i th reflecting signal. We define the differential vector as \mathbf{v}_Δ , where $[\mathbf{v}_\Delta]_i = [\mathbf{v}_x]_i - [\mathbf{v}_x]_{i+1}$. When $i > N_x$, $[\mathbf{v}_\Delta]_i \approx 0$, while $i \leq N_x$, $[\mathbf{v}_\Delta]_i \gg 0$. Typically, we have $N_x \ll N$. Calculate the average of the latter half of \mathbf{v}_Δ as

$$\bar{v} = \sum_{k=\lfloor (N-1)/2 \rfloor}^{N-1} [\mathbf{v}_\Delta]_k / (N - \lfloor (N-1)/2 \rfloor), \quad (46)$$

where $\lfloor \cdot \rfloor$ is the floor function. Here, \bar{v} shall be an extremely small value approaching 0. Therefore, according to the maximum likelihood criterion, N_x can be estimated as

$$\hat{N}_x = \arg \max_i [\mathbf{v}_\Delta]_i > (1 + \varepsilon) \bar{v}, \quad (47)$$

where ε is a parameter used to avoid false estimation due to the small error. In this paper, we set $\varepsilon = 1$.

APPENDIX C

DERIVATION OF (33)

In the local coordinate, construct the ellipsoid by setting BS and UE as the focuses. The location of BS in the local coordinate is $(0, 0, 0)$. The location of the scatterer is the intersection between the radial ray pointing at $\tilde{\mathbf{p}}_{R,l}^U = (\tilde{\varphi}_l, \tilde{\theta}_l)$ and the ellipsoid. Therefore, we can construct the equation set as

$$\begin{cases} \frac{(x_n - c)^2}{a^2} + \frac{y_n^2 + z_n^2}{b^2} = 1 \\ y_n = x_n \tan \tilde{\varphi}_l \\ z_n = \sqrt{(x_n^2 + y_n^2 + z_n^2)} \cos \tilde{\theta}_l \end{cases}, \quad (48)$$

where $a = \frac{\hat{r}_{n_f, n_r}^l}{2}$, $c = \frac{r_{n_f, n_0}^0}{2}$, and $b^2 = a^2 - c^2$. By solving (48), we can obtain (33).

APPENDIX D

DERIVATION OF (37)

According to (36), we obtain

$$\ln p_{\mathbf{h}}(\mathbf{h}) = -N_c M_s \ln(\pi \sigma_N^2) - \frac{1}{\sigma_N^2} \sum_{n,m}^{N_c M_s} |h_{n,m} - B_{n,m,k}|^2. \quad (49)$$

Then, the first derivative of $\ln p_{\mathbf{h}}(\mathbf{h})$ is obtained as

$$\frac{\partial \ln p_{\mathbf{h}}(\mathbf{h})}{\partial r_k} = \frac{1}{\sigma_N^2} \sum_{n,m} \left\{ \frac{(h_{n,m} - B_{n,m,k})}{\sigma_N^2} \frac{\partial(B_{n,m,k})^*}{\partial r_l} + \frac{\partial B_{n,m,k}}{\partial r_l} (h_{n,m}^* - B_{n,m,k}^*) \right\}. \quad (50)$$

Since we have

$$\frac{\partial(B_{n,m,k})^*}{\partial r_l} = \left(\frac{\partial B_{n,m,k}}{\partial r_l} \right)^*, \quad (51)$$

$$\frac{\partial B_{n,m,k}}{\partial r_l} = \left(-j2\pi n \Delta f \frac{1}{c} \right) B_{n,m,k}, \quad (52)$$

we can then obtain

$$\frac{\partial \ln p_{\mathbf{h}}(\mathbf{h})}{\partial r_k} = -\frac{1}{\sigma_N^2} \sum_{n,m} 2\text{Re} \left\{ \left(j2\pi n \Delta f \frac{1}{c} \right) h_{n,m}^* B_{n,m,k} \right\}. \quad (53)$$

Based on (52) and (53), we can obtain the second-order derivative of $\ln p_{\mathbf{h}}(\mathbf{h})$ as

$$\begin{aligned} \frac{\partial^2 \ln p_{\mathbf{h}}(\mathbf{h})}{\partial^2 r_l} &= -\frac{2}{\sigma_N^2} (2\pi n \Delta f \frac{1}{c})^2 \sum_{n,m} \text{Re} \left\{ |B_{n,m,k}|^2 + \bar{n}_{t,n,m} B_{n,m,k} \right\}. \end{aligned} \quad (54)$$

Since $B_{n,m,k} = \sqrt{P_t^U} A_k e^{j2\pi m T_s^p \tilde{f}_{d,k,m}} e^{-j2\pi n \Delta f \frac{r_k}{c}}$, we can finally obtain

$$E \left\{ \frac{\partial^2 \ln p_{\mathbf{h}}(\mathbf{h})}{\partial^2 r_k} \right\} = -\frac{P_t^U}{\sigma_N^2} 8\pi^2 \Delta f^2 \frac{1}{c^2} |A_k|^2 M_s \sum_n n^2. \quad (55)$$

REFERENCES

- [1] W. Saad, M. Bennis, and M. Chen, "A Vision of 6G Wireless Systems: Applications, Trends, Technologies, and Open Research Problems," *IEEE Network*, vol. 34, no. 3, pp. 134–142, May 2020.
- [2] W. Jiang, B. Han, M. A. Habibi, and H. D. Schotten, "The Road Towards 6G: A Comprehensive Survey," *IEEE Open Journal of the Communications Society*, vol. 2, pp. 334–366, Feb. 2021.
- [3] N. H. Mahmood, H. Alves, O. A. López, M. Shehab, D. P. M. Osorio, and M. Latva-aho, "Six key enablers for machine type communication in 6G," *2020 2nd 6G Wireless Summit, Levi, Finland*, 2020.
- [4] F. Liu, C. Masouros, A. Petropulu, H. Griffiths, and L. Hanzo, "Joint radar and communication design: Applications, state-of-the-art, and the road ahead," *IEEE Transactions on Communications*, June 2020.
- [5] X. Chen, Z. Feng, Z. Wei, P. Zhang, and X. Yuan, "Code-Division OFDM Joint Communication and Sensing System for 6G Machine-Type Communication," *IEEE Internet of Things Journal*, vol. 8, no. 15, pp. 12 093–12 105, Feb. 2021.
- [6] F. Liu, Y. Cui, C. Masouros, J. Xu, T. X. Han, Y. C. Eldar, and S. Buzzi, "Integrated Sensing and Communications: Toward Dual-Functional Wireless Networks for 6G and Beyond," *IEEE Journal on Selected Areas in Communications*, vol. 40, no. 6, pp. 1728–1767, June 2022.
- [7] Z. Feng, Z. Wei, X. Chen, H. Yang, Q. Zhang, and P. Zhang, "Joint Communication, Sensing, and Computation Enabled 6G Intelligent Machine System," *IEEE Network*, vol. 35, no. 6, pp. 34–42, Nov. 2021.
- [8] J. A. Zhang, F. Liu, C. Masouros, R. W. Heath, Z. Feng, L. Zheng, and A. Petropulu, "An overview of signal processing techniques for joint communication and radar sensing," *IEEE Journal of Selected Topics in Signal Processing*, vol. 15, no. 6, pp. 1295–1315, Sept. 2021.

- [9] X. Yuan, Z. Feng, J. A. Zhang, W. Ni, R. P. Liu, Z. Wei, and C. Xu, "Spatio-Temporal Power Optimization for MIMO Joint Communication and Radio Sensing Systems With Training Overhead," *IEEE Transactions on Vehicular Technology*, vol. 70, no. 1, pp. 514–528, Jan. 2021.
- [10] S. A. Hassani, B. van Liempd, A. Bourdoux, F. Horlin, and S. Pollin, "Joint in-band full-duplex communication and radar processing," *IEEE Systems Journal*, pp. 1–9, July 2021.
- [11] J. A. Zhang, K. Wu, X. Huang, Y. J. Guo, D. Zhang, and R. W. Heath, "Integration of radar sensing into communications with asynchronous transceivers," *IEEE Communications Magazine*, pp. 1–7, Aug. 2022.
- [12] H. Kuschel, D. Cristallini, and K. E. Olsen, "Tutorial: Passive radar tutorial," *IEEE Aerospace and Electronic Systems Magazine*, vol. 34, no. 2, pp. 2–19, Feb. 2019.
- [13] W. Yuan, N. Wu, B. Etzlinger, Y. Li, C. Yan, and L. Hanzo, "Expectation-maximization-based passive localization relying on asynchronous receivers: Centralized versus distributed implementations," *IEEE Transactions on Communications*, vol. 67, no. 1, pp. 668–681, Jan. 2019.
- [14] K. Qian, C. Wu, Y. Zhang, G. Zhang, Z. Yang, and Y. Liu, "Widar2.0: Passive human tracking with a single wi-fi link," *Proceedings of the 16th Annual International Conference on Mobile Systems, Applications, and Services*, p. 350–361, 2018.
- [15] Z. Ni, J. A. Zhang, X. Huang, K. Yang, and J. Yuan, "Uplink sensing in perceptive mobile networks with asynchronous transceivers," *IEEE Transactions on Signal Processing*, vol. 69, pp. 1287–1300, Feb. 2021.
- [16] Y. Zeng, D. Wu, J. Xiong, E. Yi, R. Gao, and D. Zhang, "FarSense: Pushing the Range Limit of WiFi-Based Respiration Sensing with CSI Ratio of Two Antennas," *Proc. ACM Interact. Mob. Wearable Ubiquitous Technol.*, vol. 3, no. 3, Sept. 2019.
- [17] Y. Zeng, D. Wu, J. Xiong, J. Liu, Z. Liu, and D. Zhang, "Multisense: Enabling multi-person respiration sensing with commodity wifi," *Proc. ACM Interact. Mob. Wearable Ubiquitous Technol.*, vol. 4, no. 3, Sept. 2020.
- [18] X. Li, J. Andrew Zhang, K. Wu, Y. Cui, and X. Jing, "CSI-Ratio-based Doppler Frequency Estimation in Integrated Sensing and Communications," *IEEE Sensors Journal*, pp. 1–10, Sept. 2022.
- [19] X. Chen, Z. Feng, Z. Wei, F. Gao, and X. Yuan, "Performance of Joint Sensing-Communication Cooperative Sensing UAV Network," *IEEE Transactions on Vehicular Technology*, vol. 69, no. 12, pp. 15 545–15 556, Dec. 2020.
- [20] W. H. T. Rodger E. Ziemer, *Principles of Communications*, 7th ed. Wiley, 2014.
- [21] Y. S. Cho, J. Kim, W. Y. Yang, and C. G. Kang, *MIMO-OFDM Wireless Communications with MATLAB*. Wiley Publishing, 2010.
- [22] Y. Gao, J. Xue, Y. Chang, and Y. Zhang, "An MDL-MUSIC joint time delay estimation method for LTE PRS," pp. 84–89, Oct. 2017.
- [23] M. Haardt, M. Pesavento, F. Roemer, and M. Nabil El Korso, "Chapter 15 - subspace methods and exploitation of special array structures," in *Academic Press Library in Signal Processing: Volume 3*, A. M. Zoubir, M. Viberg, R. Chellappa, and S. Theodoridis, Eds. Elsevier, 2014, vol. 3, pp. 651–717.
- [24] J. A. Zhang, X. Huang, Y. J. Guo, J. Yuan, and R. W. Heath, "Multibeam for joint communication and radar sensing using steerable analog antenna arrays," *IEEE Transactions on Vehicular Technology*, vol. 68, no. 1, pp. 671–685, Jan. 2019.
- [25] G. C. Charles K. Chui, *Kalman Filtering: with Real-Time Applications*. Springer International Publishing, 2017.
- [26] B. C. Levy, "Principles of signal detection and parameter estimation," *Springer Science & Business Media*, 2008.
- [27] "Physical layer procedures for control," *3GPP Technical Specification 38.213 V17.3.0*, Sept. 2022.